PAPER • OPEN ACCESS

Metamaterial boat fenders with supreme shape recovery and energy absorption/dissipation via FFF 4D printing

To cite this article: Mahdi Bodaghi *et al* 2023 *Smart Mater. Struct.* **32** 095028

View the article online for updates and enhancements.

Metamaterial boat fenders with supreme shape recovery and energy absorption/dissipation via FFF 4D printing

Mahdi Bodaghi[1,*] , **Naser Namvar**[2] , **Armin Yousefi**[1] , **Hadi Teymouri**[2], **Frédéric Demoly**[3,4] **and Ali Zolfagharian**[5]

[1] Department of Engineering, School of Science and Technology, Nottingham Trent University, Nottingham NG11 8NS, United Kingdom
[2] Department of Mechanical Engineering, University of Tabriz, Tabriz, Iran
[3] ICB UMR 6303 CNRS, Belfort-Montbeliard University of Technology, UTBM, 90010 Belfort Cedex, France
[4] Institut universitaire de France (IUF), Paris, France
[5] School of Engineering, Deakin University, Geelong, Victoria 3216, Australia

E-mail: mahdi.bodaghi@ntu.ac.uk

CrossMark

Abstract

In maritime transportation, a fender acts like a bumper to absorb the kinetic energy of a boat berthing against a jetty, pier wall, or other boats. They have high energy absorption and low reaction forces, preventing damage to boats and berthing structures. The aim of this paper is to introduce a novel conceptual design for a new class of lightweight boat-fendering systems with superior energy absorption/dissipation and shape recovery features. Different metamaterials with honeycomb, re-entrant, and re-entrant chiral auxetic patterns are designed in the form of boat fender panels, and their thermo-mechanical behaviors are analyzed experimentally and numerically. A finite element modeling (FEM) is developed to investigate the compressive behaviors of boat fenders. Some of designs are 4D printed by fused filament fabrication of shape memory polylactic acid polymers and then tested thermo-mechanically. A good correlation is observed between numerical and experimental results, supporting the FEM accuracy. Results reveal that proposed boat fenders have considerable energy absorption/dissipation along with the capability to fully recover plastic deformations by simply heating up. The excellent mechanical property recovery of the proposed boat-fendering system is also shown under cycling loadings. Due to the absence of similar conceptual designs, models, and results in the specialized literature, this paper is expected to be instrumental towards 4D printing novel boat fenders with supreme energy absorption/dissipation and shape recovery properties promoting sustainability.

(Some figures may appear in colour only in the online journal)

---

* Author to whom any correspondence should be addressed.

1. Introduction

Crashworthiness, known as one of the most significant features of structures, provides them with the ability to absorb impact energy, with applications in automobile, aerospace, defense, and marine applications [1–5]. To guarantee passengers' safety, it is vital to design and implement energy-absorbing structures in transportation vehicles. Vehicles contain numerous structural elements. Considering car bumpers as an example, this part plays a crucial role in absorbing the impact load while hitting an external object. Thus, this element can simply provide passengers' safety by considerably absorbing kinetic energy during a car crash [6, 7]. Bumper-like structures with an energy absorption function are also employed in the marine industries and are known as boat-fendering structures.

Designing and manufacturing novel structures using additive manufacturing (AM) has gained significant attention due to its potential in terms of shape or structure complexity for innovative solutions [8]. Mechanical metamaterials refer to artificial cellular materials demonstrating eccentric properties that are not available in natural materials [9, 10]. Negative Poisson's ratio [3, 11], tunable load-bearing capacity [12], tunable negative thermal expansion [13], negative stiffness [14], and distinctive dynamic properties in many frequency ranges [15] are a few of these remarkable mechanical properties. Their extraordinary characteristics are derived from their structural geometries, not their chemical compositions [16]. Their small-scale geometry determines the characteristics of mechanical metamaterials at larger sizes [17]. The advancement of metamaterials has been sped up by the development of AM (often known as 3D printing). 3D printing has been widely utilized for fast prototyping across various fields. This method enables the manufacturing of complex structures for different objects, for example, metamaterials with high energy absorption capabilities. The 3D printing technology has shown remarkable potential because of its advantages over conventional methods, including reasonable manufacturing costs and time savings [18].

Recently and beyond AM, a new manufacturing paradigm has been introduced to give life to 3D objects and structures, namely 4D printing. It combines AM and smart or active materials to produce objects with shape and/or property changes once stimulated by energy (e.g. heat, humidity, light, electric/magnetic field, etc) [19–25]. Currently, 4D printing, which is still in its infancy, has emerged as an intriguing subfield of AM, attracting much attention across various fields. In 4D printing technology, shape memory polymers (SMPs), such as polylactic acid (PLA), are common materials to fabricate shape memory structures. SMPs may hold a temporary shape via shape programming and recover the original shape in response to an external stimulus, such as heat. Recent engineering applications have employed this shape memory feature [26–29]. For example, Tao *et al* [24] proposed multi-stable 4D printed metamaterial designs with wide application robots, smart damping interfaces and adaptable aerospace structures.

Lately, several researchers have attempted to investigate the shape recovery properties of different structures with complex geometries [30–32]. Namvar *et al* [30] proposed three architected metamaterials, including hexagonal, re-entrant, and AuxHex, with the aid of 4D printing for energy absorption applications with shape recovery properties. Results indicated that re-entrant lattice structures provided higher energy absorption capacity compared to the other proposed designs. Hamzehei *et al* [31] introduced lattice structures with zero Poisson's ratio (ZPR) and illustrated the shape recovery capacity of metamaterials via a heating–cooling test. Results revealed that the structure could fully recover its initial shape. The novel ZPR lattice was compared with conventional 3D re-entrant metamaterials for energy absorption capacity, presenting considerable mechanical performance. Sharma and Hiremath [32] designed and fabricated lattice structures bio-inspired by sea sponges. The structure combines hard (PLA) and soft (thermoplastic polyurethane) materials to increase the energy absorption capability. Compressive in-plane and out-plane loading tests were carried out to investigate the stability and energy absorption features under different loading conditions.

Most of the research done so far has been led on structures with uniformly sized and constructed unit cells. However, a new class of lattice structures known as functionally graded (FG) structures with a gradually varying distribution of unit cells has recently been introduced [33–35]. Regarding the absorbing energy, graded structures outperform uniform structures due to their unique mechanical characteristics [36]. According to Li *et al* [37], linear-graded honeycombs are better at absorbing energy while being rapidly crushed than non-graded unit cells. The graded metamaterials could improve mechanical characteristics under blast loading and show impact mitigation and energy absorption capacity [36]. Most of the research has been devoted to constructing 2D-graded metamaterials. Hamzehei *et al* [38] created 2D bioinspired ZPR metamaterials in this regard for applications including energy absorption and stability. In order to demonstrate higher energy absorption capacity under high-velocity impacts, Li *et al* [37] developed segmented, graded hierarchical honeycomb structures with triangle substructures and graded hierarchical structures with the Kagome pattern. The in-plane crushing performance was investigated by employing the finite element modeling (FEM). They introduced the concept of cyclic graded structures that can improve the energy absorption capacity of new multifunctional structures.

One of the main applications of energy absorber structures in the marine industry is for boat-fendering systems. A fender is a bumper-like structure employed to absorb the kinetic energy of a boat/vessel berthing against a jetty, pier wall, or other boats/vessels/pier wall, see figure 1. The boat-fendering system plays a vital role in absorbing the collision energy, preventing any damage to boats/vessels/pier walls, and mitigating unwelcome shocks to the passengers. In order to optimize the energy absorption capability and strength of fendering

Figure 1. Conventional boat fenders: (a) side view and (b) front view.

systems, foam-filled fenders, hydro-pneumatic fenders, and buckling column rubber fenders are employed [39].

Fan *et al* [40] proposed a novel fender system for bridges consisting of steel and concrete to outweigh the limitations of traditional fender systems. The first panel was reinforced concrete with an inner steel panel to help absorb the impact energy. Also, pneumatic fenders were proposed by Sakakibara and Kubo [41]. They calculated fender loads, like deflection and reaction forces, by measuring the inner air pressure of the pneumatic fenders. Because of their cost-effectiveness, elastomeric foams, rubber, and springs are also used as energy-absorbing components [42]. Flexible fenders are often used for commercial boats of all sizes and hull types [39]. Flexible energy absorbers have been considered as a good choice for low-energy shocks due to the elastic properties of the fender system and the berthing structures [43]. However, plastic deformations as permanent distortion can occur when the boat fender experiences compressive stresses exceeding the material yield stress. This residual plastic deformation is irreversible. It means the boat fender must be replaced with a new one that is not sustainable, increasing the material waste, energy usage for manufacturing, and labor cost. Therefore, designing recoverable boat fenders and removing the need for part replacement could promote sustainability and lower waste of materials, time, energy, and labor needs.

The main objective of the present study is to introduce a novel conceptual design of small-scale mechanical metamaterials for a new class of lightweight boat-fendering systems with supreme energy absorption/dissipation and shape recovery features. Figure 2 presents an overview of the proposed work, starting from the design of boat-fendering structures and their simulation, 4D printing, and mechanical testing. Lattice-based metamaterials with various patterns, including functional gradients, are designed in a cylindrical panel form. The mechanical performance of the developed metamaterial boat-fendering structures is investigated numerically and experimentally under compressive loadings. In this respect, a FEM is developed to predict the mechanical behaviors of metamaterials under compression. As a feasibility study, a few designs are 4D printed by fused filament fabrication (FFF) method using PLA SMPs. Samples are tested by applying

a large compressive loading and unloading loop and experiencing elastic–plastic deformations. Their shape recovery is also tested by simply heating them at the end of the loading–unloading step. Experiments reveal that not only do the new metamaterial boat fenders possess a high energy absorption capability, but they also can recover the mechanically induced plastic deformation and return to their original shape by simply heating. The numerical results are then compared with experimental data, showing the high accuracy of the developed FEM. The experimentally validated FEM is further implemented to understand the mechanical behaviors of the proposed metamaterial boat fenders and to show their mechanical performance. The metamaterial-structural model, concepts, and results supplied in this paper are expected to open a new avenue for designing advanced boat-fendering systems with exceptional energy absorption and shape recovery features promoting sustainability. This paper is structured as follows. In the introduction, the conventional boat fendering system and the novel type of mechanical metamaterials are presented. In section 2.1, PLA and shape memory recovery programming is discussed. After the introduction of materials, the mechanical properties are characterized in sections 2.2 and 2.3. In sections 2.4 and 2.5, the novel boat fender computer-aided design (CAD) files are presented, and the 3D printed structures are illustrated. Section 3 discusses the details of the finite element method to analyze the energy absorption capability and deformation of boat fenders subjected to impact load. Section 4 presents both experimental and numerical results for design. In this section, the verification between experimental and numerical investigation is presented, and the numerical results for further designs are illustrated. Discussion and conclusions are finally presented in sections 5 and 6, respectively.

2. 4D materials and printing

2.1. PLA cold programming and shape recovery

PLA is a thermoplastic SMP and possesses excellent shape memory properties. It can be programmed via cold and hot programming protocols and returned to its original shape by heating. In this paper, SMPs are used to fabricate metamaterial
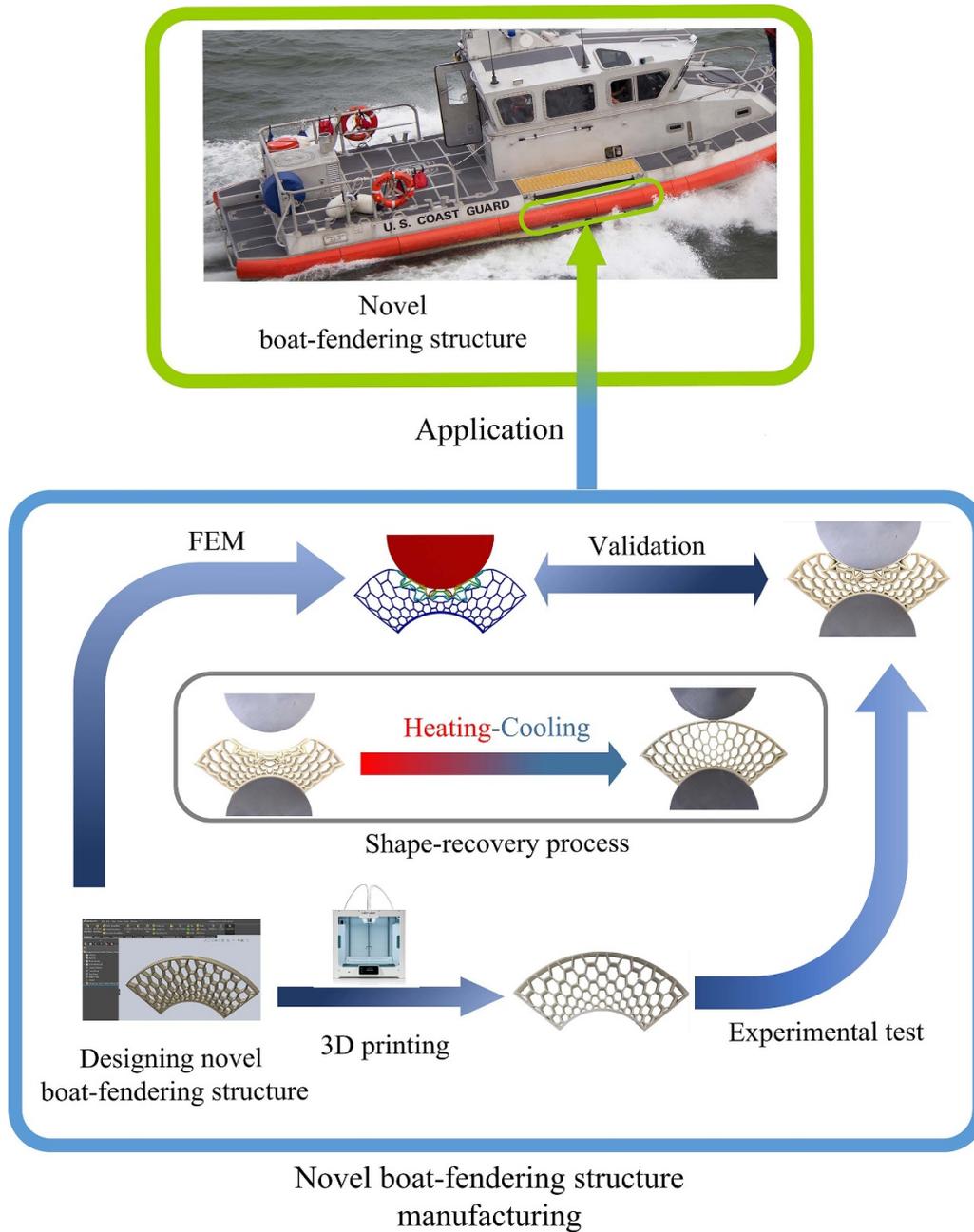
Figure 2. Proposed design, simulation, and manufacturing loop of a shape-changing boat-fendering system.

boat fenders in a panel shape, and they usually experience an automatic cold programming protocol during their service. Here, the cold programming steps are described in figure 3 as part of the conceptual design of shape memory boat fenders. The boat fender is loaded at ambient temperature, which is below the glass transition temperature, and experiences an elastic deformation followed by a strain-hardening plastic deformation (step 1). The polymer chains progressively realign in the loading direction and store mechanical energy. When SMP is unloaded, a rapid spring back releases a portion of the stored energy (step 2). However, the material does not fully return to its original shape, and there will be some residual plastic deformations. Step 3 is the shape-recovery

process, in which the SMP boat-fendering structure is heated above T_g and can recover its initial shape. Finally, by cooling the structure to RT, it fully returns to its original shape (see step 4) [44].

2.2. Dog-bone 3D printing

First, experiments are made using FFF technique to print small-scale mechanical metamaterial designs. To do so, PLA filaments (Recreus Inc., Elda, Spain) with a diameter of 2.85 mm and a T_g of 65 °C are utilized with a Ultimaker S5 machine. Raw filaments are heated in a liquefier chamber within the 3D printer until they reach a semi-molten phase.
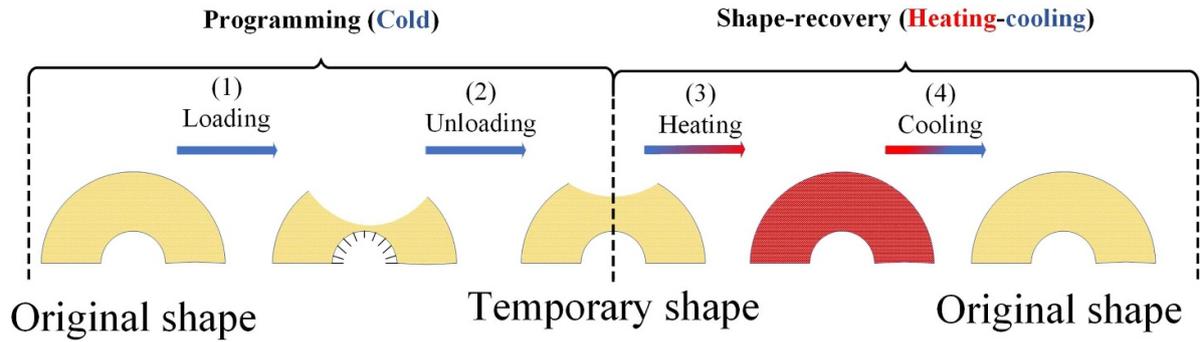
Figure 3. Description of the cold programming and shape recovery for SMP-based absorbing structures: (1) loading, (2) unloading at room temperature, (3) heating above T$_g$, and (4) cooling to RT.
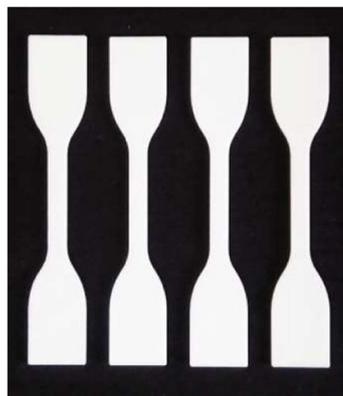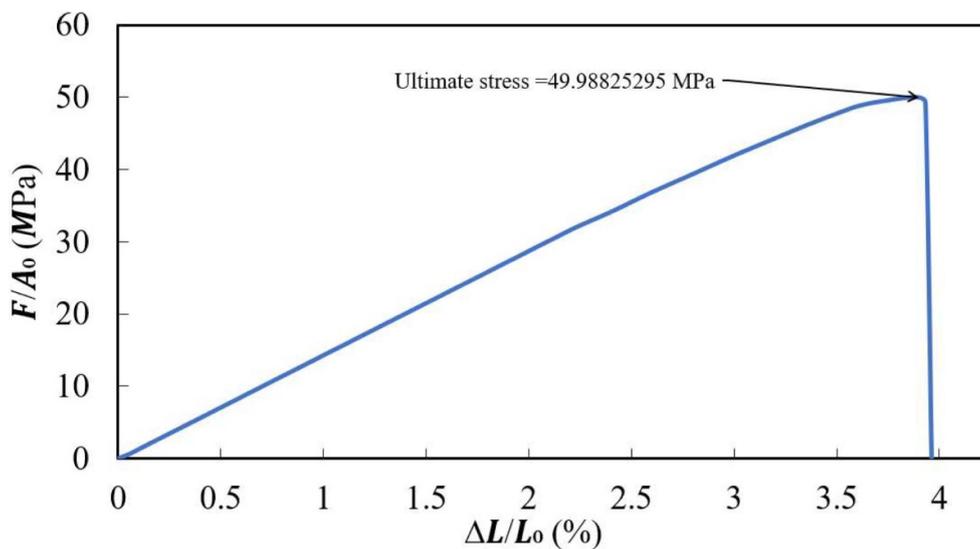
Figure 4. (a) Tensile test specimens, (b) Shimadzu AGS-X tensile testing machine, and (c) stress–strain curve of the 3D printed PLA dog-bone specimen.

Then, heated filaments are deposited through a nozzle in a horizontal, layer-by-layer arrangement from the bottom to the top of a heated bed surface. The bed and nozzle temperatures are set 40 °C and 200 °C, respectively. A layer height of 0.2 mm, 100% density, and a printing speed of 20 mm s^{-1} were adopted. Four dog-bone tensile samples were 3D printed in accordance with ASTM standard D638 (TYPE IV) in order to determine mechanical characteristics of the PLA utilized in this investigation. The raster angle is set at 0° implying that the dog-bone sample is filled with a perimeter raster in which the raster is aligned with the length of the gauging section. These testing conditions are applied for each specimen to ensure the validity of test findings. The tensile test specimens and tensile testing machine are shown in figures 4(a) and (b), respectively.

2.3. Mechanical behaviors of PLA

The tensile test is carried out uniaxially on the dog-bone samples using the Shimadzu AGS-X (Kyoto, Kyoto Prefecture, Japan). A constant crosshead speed of 15 mm min^{-1} and a load cell of 50 kN are considered at RT. The strain rate is low (0.5% s^{-1}) [45, 46], in the range of rates that a boat fender usually experiences [45, 46], and it is classified as quasi-static.

The tensile stress–strain curve of the PLA material is shown in figure 4(c), ΔL, *F, L_0,* and A_0 stand for displacement, force, initial length, and initial cross-sectional area, respectively. Similar results of Young's modulus of 1.43 GPa and Poisson's ratio of 0.32 are achieved in all four dog-bone PLA samples. Figure 4(c) demonstrates that the PLA material behavior is elastoplastic. Plasticity occurs at 2.2% strain due to the change in the slope of the stress–strain curve following a residual deformation that remains upon unloading. It is seen that PLA experiences maximum stress of 49.99 MPa and then breaks down after a short plateau.

2.4. Metamaterial lattice designs

The efficiency of a metastructure is significantly influenced by the geometrical factors of its unit cells. Numerous investigations have been carried out to determine how geometrical factors affect the capacity of cellular metamaterial structures to absorb energy [47–49]. For instance, Yang *et al* [50] claimed that the negative Poisson's ratio of re-entrant lattice depends on the internal angle. When the re-entrant angle (inside angle) is obtuse, the re-entrant looks like a honeycomb, and therefore, the Poisson's ratio becomes positive. The maximum auxeticity was observed in mechanical metamaterials composed of thin struts with a horizontal-to-oblique strut length ratio of 2 and a re-entrant angle ranging from 60° to 70°. According to Wang *et al* [51], Young's modulus rises, but the auxeticity ultimately declines for re-entrant lattice structures by increasing the wall thickness. It was also demonstrated that when relative density rises, the ability to absorb energy increases. As a result, increasing cell wall thickness in a re-entrant structure increases the energy absorption capacity and relative density.

This study considers common cellular metamaterial designs known as honeycomb lattice, re-entrant lattice, and re-entrant chiral auxetic (RCA) to develop novel boat fenders with remarkable energy absorption. In this regard, apart from the honeycomb lattice, six metamaterial designs with FG patterns are proposed and expected to result in excellent energy absorption capacities. CAD models of the metamaterial structures were prepared using SOLIDWORKS (Dassault Systèmes, France). They are named FG honeycomb I, FG honeycomb II, FG re-entrant I, FG re-entrant II, FG RCA I, and FG RCA II, as displayed in figure 5.

2.5. 3D printing and testing of metamaterial

Among the proposed CAD models of the metamaterial structures, three geometric definitions are 3D printed with FFF technique and PLA material and then tested under compressive

loading. The CAD models in native format are converted into STL files from SOLIDWORKS software. They are then sliced in Cura (Ultimaker, The Netherlands) software and verted in G-code instructions to be considered in the 3D printer. Figure 6 shows the 3D-printed structures. In order to model the berthing process, a solid semi-circle indenter is 3D printed and then attached to the top of the compression testing machine's plate to carry out a compression test on the 3D-printed lattices. A solid panel foundation is also 3D printed and placed on the bottom plate, while the metamaterial lies on it while testing. The 3D-printed novel boat fenders in cylindrical panel form are examined under a quasi-static displacement-controlled compression test (with a maximum stroke of 30 mm). The test is carried out with a constant crosshead velocity of 16 mm min^{-1} at room temperature (23 °C). It results in a strain rate of 0.5% s^{-1} that falls into the range of boat fender loading rates [46]. The shape recovery of the boat-fendering structure is also checked by heating the samples to 85 °C, which is 20 °C above the glass transition temperature, followed by cooling down.

3. FEM

Digital models designed using SOLIDWORKS in the form of Parasolid files are imported to the simulation software Abaqus (V.6.14, Dassault Systèmes, France). The objective of the simulation is to analyze the mechanical behaviors of metamaterial structures under a loading–unloading loop and validate them with experimental observation.

This section is dedicated to presenting the different steps of numerical modeling in detail. First, based on the stress–strain curve of the printed dog-bone specimen (figure 4(c)), an elastic–plastic model is assumed to simulate the behavior of the designed boat-fendering structures under compression. In this regard, the stress–strain data is imported to Abaqus by calibrating the material model. An elasto-plastic model is used to simulate the compression test. Moreover, the density and Poisson's ratio of PLA are set to 1240 kg m^{-3} and 0.32. The experimental setup is completed with the assembly modulus in the next step. It is worth mentioning that the upper indenter and the lower foundation are assumed to be rigid bodies. The meshed structure is presented in figure 7. As illustrated, a linear tetrahedron element of type C3D4 is used to mesh the metamaterial models; a linear hexahedron element type C3D8R is used for the rigid body. The element size is reduced to reach a high level of accuracy, and the force–displacement curves converge. In all models, the accuracy of the FEM analysis results can be ensured by using an average mesh size of 0.8 mm. A constant velocity of 16 mm min^{-1} is assigned to the top (movable) platen, whilst all the rotational and translational freedoms of the bottom platen are constrained (i.e. fixed). The upper indenter can move freely in the *Y* direction, although it is restricted in *X* and *Z* directions to accurately replicate the experimental test. Surface-to-surface contacts are used to simulate the interaction between the cell walls of the structure themselves as well as the rigid indenter and the model during compression. In the 'Interaction module', the tangential contact is defined by penalty formulation and the normal contact
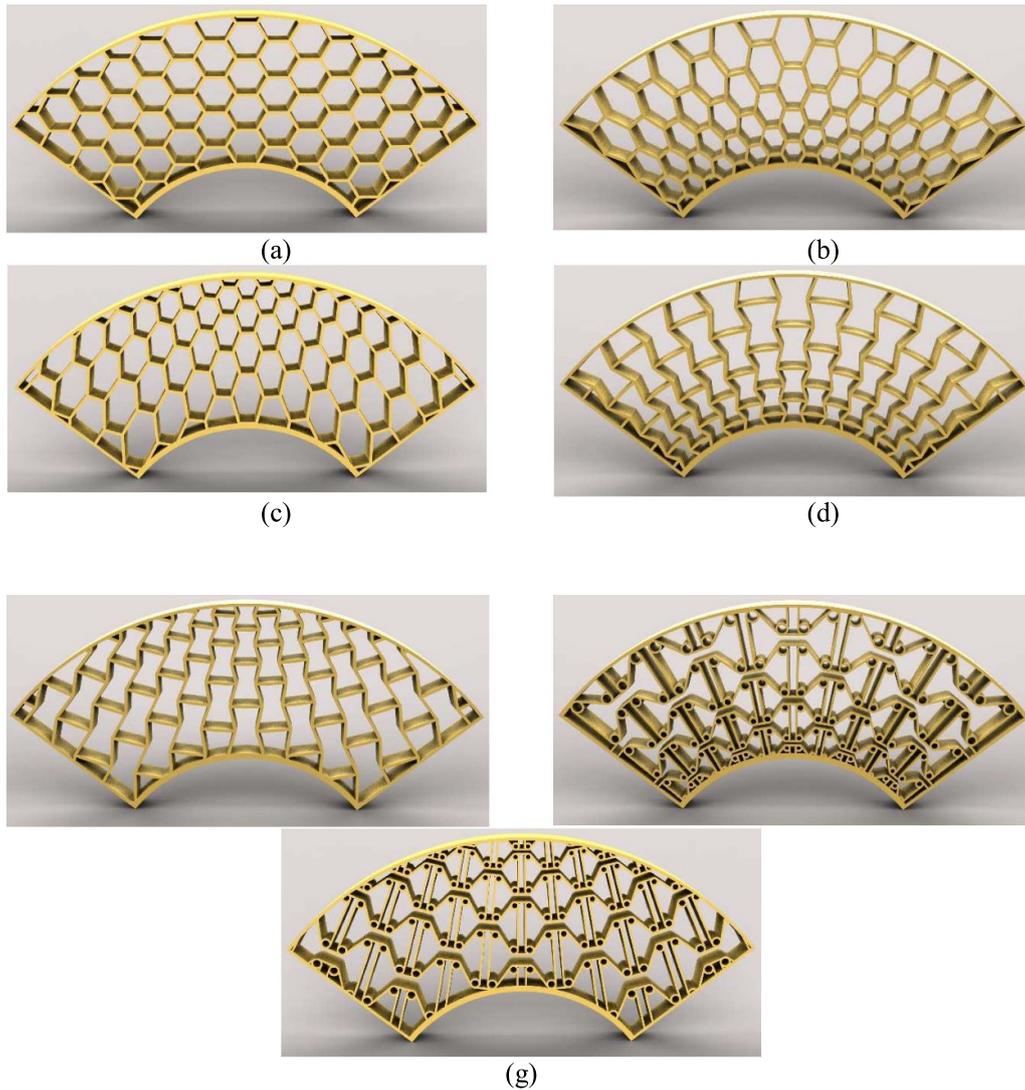
Figure 5. 3D CAD model of different lattice structures investigated in this study: (a) uniform honeycomb, (b) FG honeycomb I, (c) FG honeycomb II, (d) FG re-entrant I, (e) FG re-entrant II, (f) FG RCA I, and (g) FG RCA II.

is defined as 'Hard' contact. It is worthwhile to note that simulation of the heating–cooling process requires implementing an SMP constitutive model, which is beyond the scope of this work and would be considered in future simulation efforts. The upper indenter is moved down during the mechanical loading step to deform lattice structures, followed by unloading until the force becomes zero. Both force and displacement are reported by defining the reference point of the upper indenter.

4. Results

4.1. Verification study

This section is devoted to comparing numerical and experimental results in the loading and unloading stage for the honeycomb metamaterials. The lattice structure configuration and force–displacement curve are compared to validate the numerical modeling. It is worth mentioning to strengthen the

logic of the group pictures in this section; first, the experimental observation of the boat fender under compression load is presented. In this regard, the start of loading, end of loading, unloading and structures after heating–cooling (shape recovery) are shown. Then different stages of deformation related to FEM are presented. Following, the force–displacement for both FEM and experiment and the energy distribution of the lattice structure are illustrated.

Different stages of experimental observation, from the start of loading, the end of loading, unloading, and heating–cooling process, are presented in figures 8(a)–(d). The counterpart of figures 8(a)–(c) is illustrated in figures 8(e)–(g), predicted by the FEM. The force–displacement responses from the experiment and modeling are also presented in figure 8(h). The dissipated energy and stored energy calculated based on the experimental force–displacement graph are finally demonstrated in figure 8(i).

The comparison of the results presented in figures 8(b), (c), (f) and (g) proves that the numerical modeling calibrated by

(a)

(b)

(c)
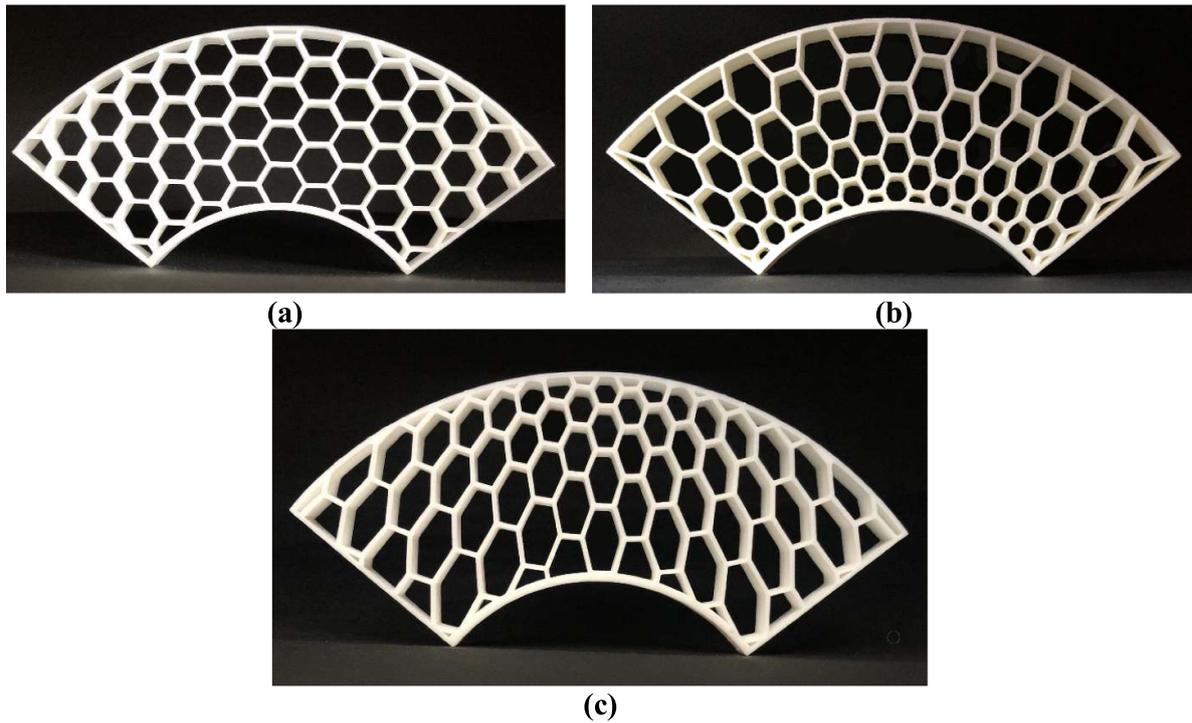
Figure 6. 3D printed structures: (a) uniform honeycomb, (b) FG honeycomb I, and (c) FG honeycomb II.
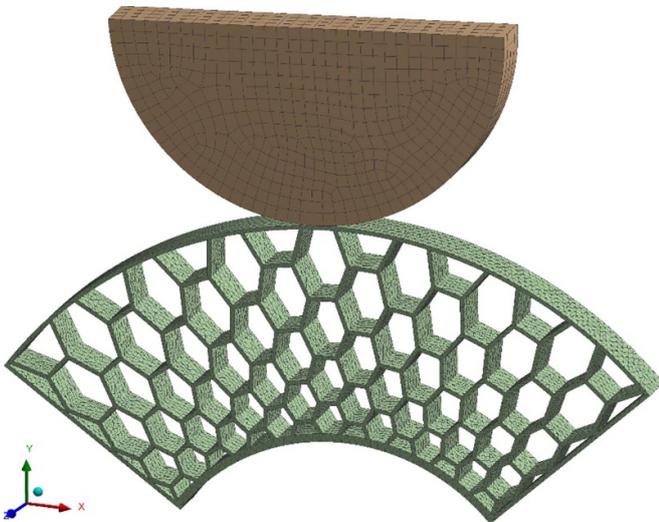
Figure 7. The lattice structure with the generated mesh.

simple tensile data from testing of 3D printed PLA can accurately predict the lattice deformation at the end of loading and unloading steps. As seen in the loading stage, the deformation mainly happens in the central area, resulting in the peanut-shaped configuration. Through the analysis of the graph in figure 8(h), it can be found that the FEM can predict the mechanical response of the honeycomb boat fender in terms of force–displacement with acceptable accuracy. The maximum difference is almost 23%. Figures 8(b), (f) and (h) demonstrate how the uniform honeycomb lattice structure tends to

stiffen when the beam-like members come into contact with one another, increasing the force level. Figure 8(h) shows that the force versus displacement has a linear trend from 0 to 2.5 mm. Then, by penetrating the upper indenter into the lattice structure, the force fluctuates versus displacement while it has a hardening behavior and rises by increasing displacement until a stroke of 25 mm. This significant fluctuation in the force–displacement curve may be due to a layer-by-layer collapse and stress concentration growing from the center. From displacement 25 mm–30 mm, the force decreases by increasing the displacement since most of the beam-like members located in the middle, along with the direction of applied displacement (that is the direction of the indenter) deform completely. The beam-like structures away from the central area are observed to deform less. Therefore, they withstand less force than those in the applied direction. Ups and downs in the force level can be related to local collapses and overall softening and hardening. Von Mises stress distribution in figure 8(f) proves that some beam members experience higher stress than the yield stress, leading to plastic deformations. During compression loading, the maximum experimental and numerical forces become 820 N and 770 N, respectively.

By unloading, the structure intends to recover its initial shape; however, it cannot be done fully. Due to plastic deformations and buckling-type instability, a mechanical hysteresis exists; therefore, the loading and unloading paths do not coincide. It is seen from the configuration of the lattice at the end of unloading that there are some residual deformations inside the structures (see figures 8(b), (f) and (h)). Figure 8 reveals that the developed FEM can accurately capture the unloading

Start of loading
(a)

End of loading
(b)

End of unloading
(c)

End of heating-cooling
(d)

Start of loading
(e)

End of loading
(f)

End of unloading
(g)

von Mises stress (MPa)

| 37.961 Max |
| 33.744 |
| 29.528 |
| 25.312 |
| 21.096 |
| 16.879 |
| 12.663 |
| 8.4466 |
| 4.2303 |
| 0.013964 Min |

(h)

(i)
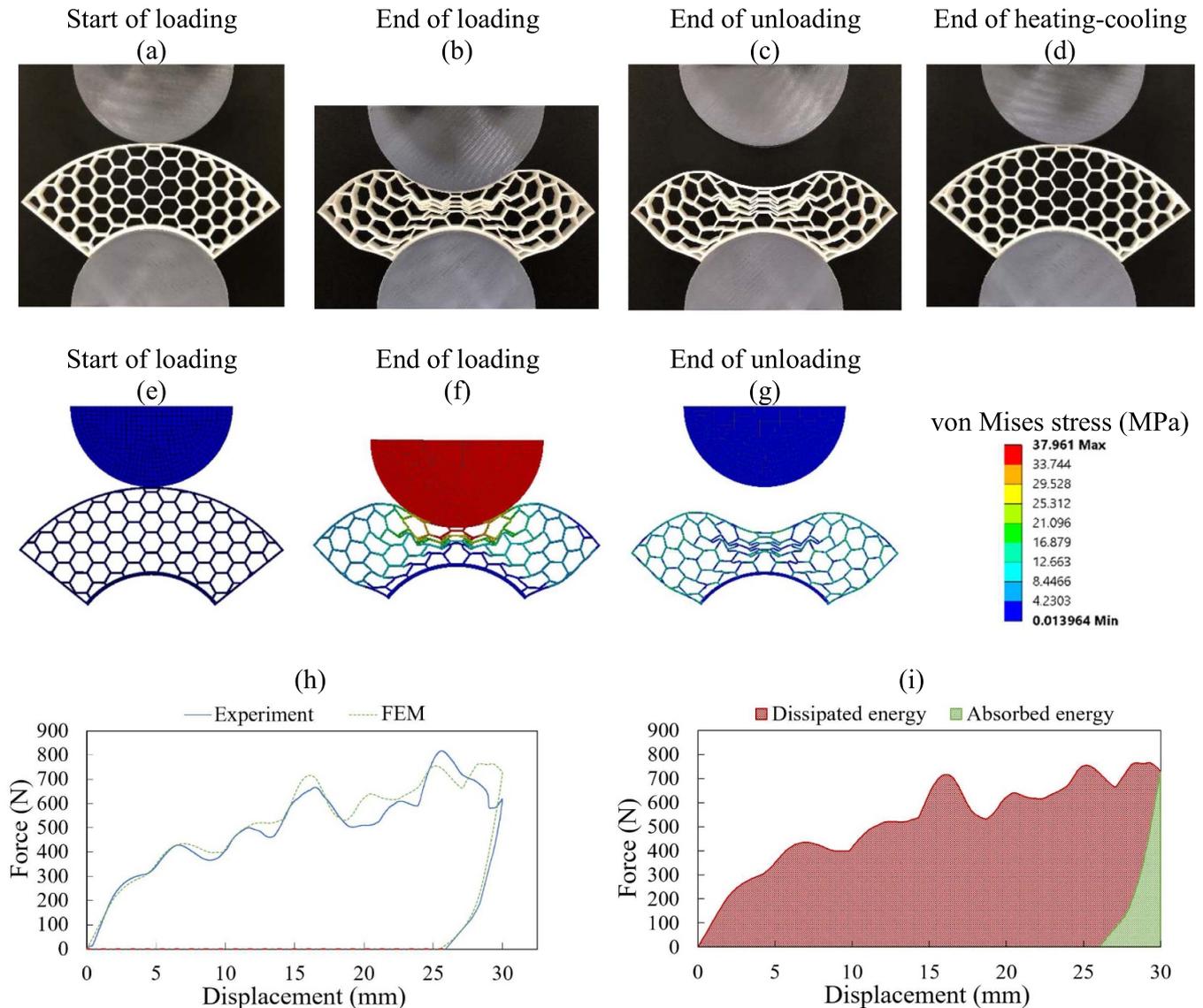
Figure 8. Uniform honeycomb: (a)–(g) experimental and computational configuration of lattice structure before loading, at the end of loading, unloading, and heating–cooling, (h) force–displacement response during loading–unloading from experiment and FEM (red dash-dotted line related to the shape-memory recovery), (i) the dissipated (red area) and absorbed energies (green area).

path, the residual deformation, and the configuration observed in the experiment. To study the shape recovery characteristics of lattice-based energy absorbers after loading–unloading at RT (23 °C), they are heated up to 85 °C, which is higher than their T_g, then cooled down to RT. The red dash-dotted line in the displacement axis is related to the heating in figure 8(d). The results show the PLA lattice's outstanding shape memory recovery feature as all the plastic deformations disappear fully upon heating.

As the boat fender structures experience an elastic–plastic behavior, the term energy absorption/dissipation is used to describe energy distribution in the structures. The energy distribution of lattice structures is crucial, mainly when used for boat fenders. In this regard, the lattice structure's energy dissipation and absorption features are analyzed, as reported in figure 8(i). The area of the loading–unloading force–displacement loop is known as the dissipated energy area (red

section); see figure 8(i). The area below the unloading curve is also known as the absorbed energy area (green section). The energy dissipation may arise from nonlinear instability due to beam-like elements' bending, buckling, plasticity, and small viscoelasticity. On the other hand, the absorbed energy is related to the bending and buckling of the beam-like structure in the elastic regime. Upon unloading the metamaterial, its beam-like structures release that portion of energy known as absorbed energy. The uniform honeycomb lattice tends to recover its initial form during the unloading, and its top central point recovers up to almost 5 mm. Figure 8(i) reveals the excellent energy dissipation of PLA and honeycombed structure that could be suitable for boat-fendering applications.

Finally, two key factors related to the shape memory behavior of PLA materials, namely shape fixity and shape recovery rate, are examined. Shape fixity assesses the specimen's capacity to fix the temporary deformation throughout the cold

Start of loading
(a)

End of loading
(b)

End of unloading
(c)

End of heating-cooling
(d)

(e)

(f)

(g)

von Mises stress (MPa)

(h)

(i)
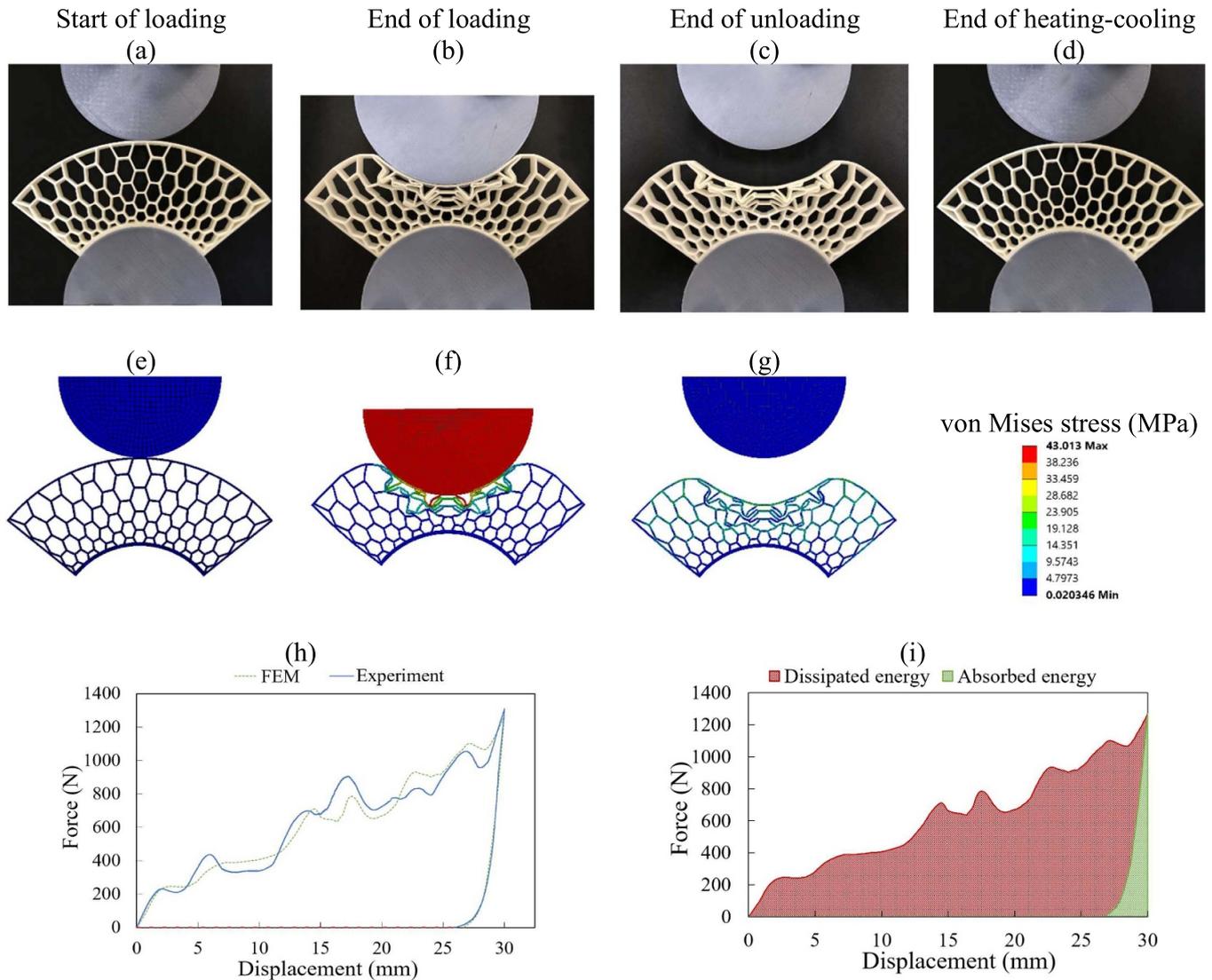
Figure 9. The counterpart of figure 8 for FG honeycomb I.

programming process. In contrast, the shape recovery rate estimates the ability of materials to return to their original shape after heating. The uniform honeycomb lattice possesses a shape fixity and shape recovery rate of 84.99% and 100%, respectively.

Figures 9 and 10 demonstrate experimental and numerical results for FG honeycomb I and II to check their performance as boat-fendering structures. Parts (a)–(c) and (e)–(g) depict the experimental and numerical configuration of lattices at RT before loading, at the end of loading, and unloading, while part (d) illustrates the configuration of the fender after heating up to 85 °C and cooling down to RT (23 °C). In addition, force–displacement responses from experiments and model prediction are presented in part (h). Finally, part (i) represents dissipated and released energies via the elastic and plastic deformation mechanism during the loading–unloading cycle.

The preliminary conclusion drawn from figures 9 and 10 is the fact that FEM calibrated via simple tensile testing data can successfully replicate the configuration of gradient lattices during the loading and unloading paths and predict their force–displacement behaviors with an acceptable degree of accuracy during both loading and unloading. As illustrated in figures 9(h) and 10(h), at the initial stage of the mechanical loading (by moving the upper indenter downwards), the force in both experiments and the FEM simulation rises linearly with the axial displacement increment. Following the linear elastic regime, the force fluctuates with an increase in displacement. Local bending and buckling appear by applying the axial compressive load to the FG honeycomb structures I and II, as seen in figures 9 and 10. Interestingly, the deformation starts from the central area with a lower density, in which the size of pores is larger. In this respect, larger deformations are observed in the upper and lower areas of FG honeycomb structures I and II, respectively, see figures 9(a)–(c) and 10(a)–(c). Comparing the configuration of these two structures at the end of loading reveals that FG honeycomb structure I experiences lower overall deformations compared to structure II. It means that a smaller number of beam-like members experience deformations
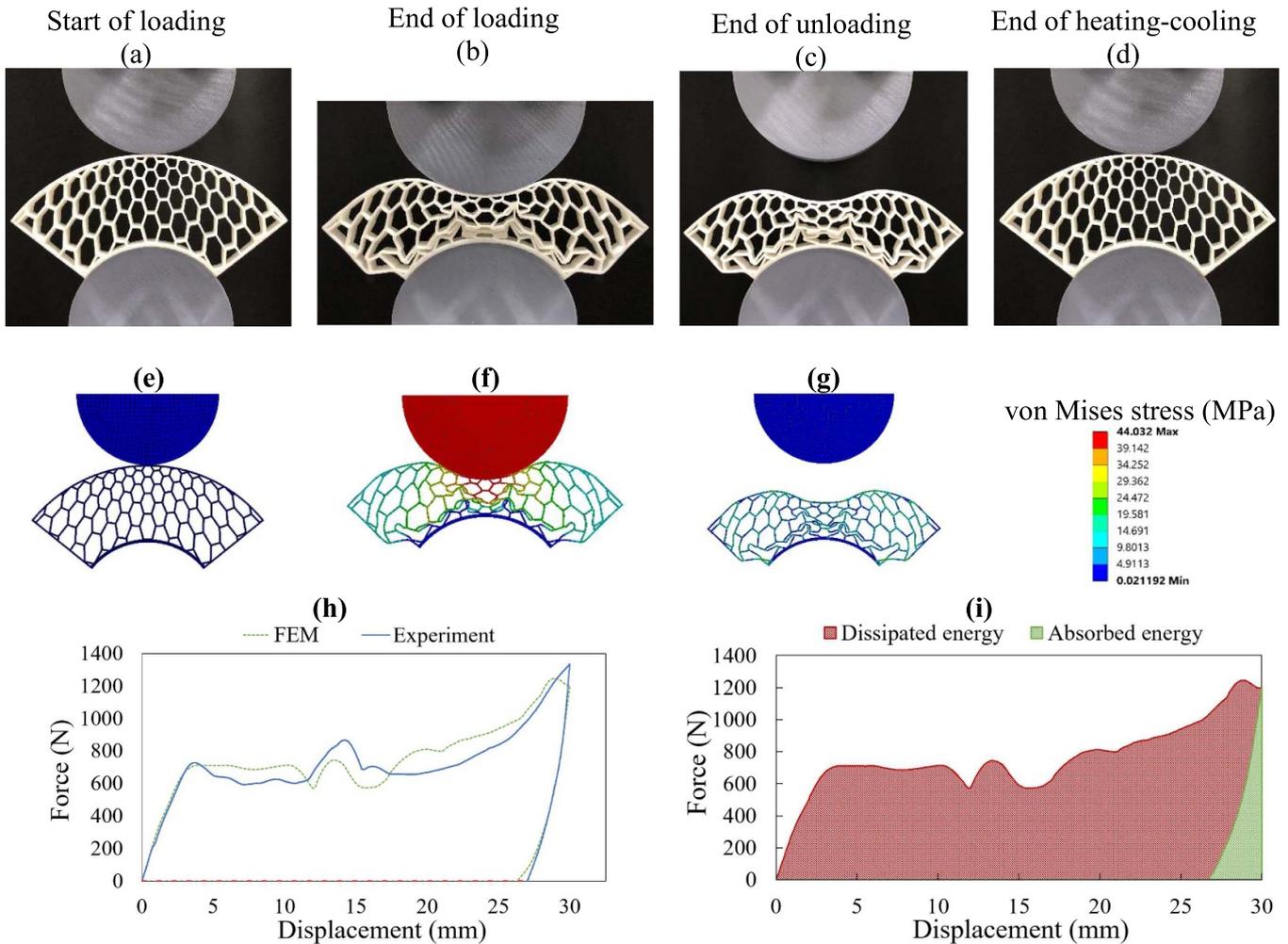
Figure 10. The counterpart of figure 8 for FG honeycomb II.

in structure I, and most of the beams around the collision just deform. However, a larger number of beam-like members deform in structure II compared to those in the uniform honeycomb and FG honeycomb I. It implies that the damage and deformation/stress can be trapped and limited by making the area close to the impact location softer. The high stress level in structure I is also limited to the collision area, while most of the beam members in structure II experience a higher level of stress (see von Mises stress contours in figures 9(f) and 10(f)).

The difference in the metamaterial collapse configurations of FG honeycomb I and II also affects their force–displacement behaviors. The results presented in figures 9(h) and 10(h) reveal that FG honeycomb structure I, with a lower density in the upper area close to the impactor location, collapses sooner at force $F = 230$ N and displacement $D = 2$ mm. After a very small softening, hardening occurs in FG honeycomb structure I, and its force–displacement graph shows a nearly increasing trend all over the loading step. On the other hand, however, it is observed that FG honeycomb structure II has a longer linear elastic behavior and then collapses at $F = 700$ N and $D = 3.4$ mm. Interestingly, FG honeycomb structure II experiences a nearly flat plateau during post-buckling and plastic deformation growth, with a peak in the

middle of loading around $D = 14$ mm. FG honeycomb structure II, with a higher peak force and nearly flat plateau, is expected to dissipate more energy compared to FG honeycomb structure I. The overall plateau with a shallow decreasing–increasing–decreasing trend in the force transforms to hardening at $D = 17$ mm. The force increases monotonically after that, almost until the end of loading. The end of the overall plateau can be associated with the start of overall densification/contact when the force increases monotonically. The densification is associated with contact happening between beam-like members, creating a denser structure. When densification occurs, the structure starts to harden. Interestingly, it is found that the force levels for both FG structures I and II are very similar ($\sim$1350 N) at the end of loading, $D = 30$ mm. A peanut-shaped configuration like what is observed for uniform honeycomb is also seen for the gradient counterpart structures.

Part (d) of figures 8–10 shows the configuration of samples after the heating–cooling process experimentally. As can be seen in part (d) of figures 8–10, lattice structures release all plastic strains and get back to their original stable shape. It confirms that the shape memory metastructures have a full recovery feature. As mentioned before, simulating the

heating–cooling operation in PLA material requires employing complex constitutive equations, which is beyond the purpose of this research and is suggested to be investigated in future studies.

Upon unloading FG honeycomb metamaterials, it is seen that the force drops drastically, and then the structure experiences a very small backward softening at a low level of force. There is a large residual plastic strain at the end of the unloading. However, it can fully be recovered once the metamaterial is heated above its transition temperature under stress-free conditions, see figures 9(h) and 10(h). FG honeycomb lattice I has a shape fixity of 88.05% and a shape recovery rate of 100%, while FG honeycomb lattice II shows a shape fixity of 90.36% and a shape recovery rate of 100%.

The results presented in figures 9 and 10 finally reveal a close computational prediction of the nonlinear mechanical behaviors in terms of hysteresis shape, residual plastic deformation, densification details, and structural configurations observed in the experiment. Furthermore, the presented results in figures 8–10 show that FG honeycomb I and II can tolerate much higher forces, about 1270 N and 1330 N, respectively, compared to uniform honeycomb lattice, which is 820 N. Although force values are different, a symmetric computational and experimental deformation pattern is observed in all three structures with respect to their vertical center line. Moreover, the developed metamaterials are promising to be used as tunnelable boat-fendering structures with recoverable energy-absorbing features. The unit cell patterns can also be used to tune and control the force–displacement behaviors. These 4D-printed tunable boat fenders with excellent energy absorption/dissipation and shape recovery have the potential to promote sustainability by removing the need for part replacement, waste of materials, time, energy and labor need.

Since several researchers [11, 52, 53] have developed analytical methods to investigate the deformation of designs presented in the present study, the cellular deformation theory is not presented here. For example, Hedayati *et al* [11] developed analytical solutions for 2D re-entrant hexagonal honeycombs, which are valid for positive (honeycomb design) to negative (re-entrant) internal cell interior angle.

4.2. Further designs

The difference between numerical and experimental results is insignificant and could be associated with the assumption of perfect geometry in the FEM. In fact, some geometric imperfections in the 3D-printed lattice structures could affect the experimental results. However, the developed FEM can reliably predict the hysteresis area, yield stress, unloading path, and deformation of metamaterial structures during loading and unloading. Consequently, the FEM developed in this work is accepted to provide an incredibly accurate simulation tool to design and analyze boat fenders further. In the following, the FEM digital tool is implemented to create other metamaterials for boat-fendering applications with higher performance in terms of energy absorption and dissipation and stress/strain level. This digital tool saves materials and energy

and eliminates the need for 3D printing and mechanical testing. Four different FG metamaterial boat fenders are designed and tested computationally. It includes two types of re-entrant metamaterial designs, namely FG re-entrant I and II, and two different models of RCA metamaterial structures, namely FG RCA I and II.

In order to strengthen the logic of the group pictures, first, the deformation of the boat fender under compression load is presented. In this regard, the start of loading, end of loading, and unloading stages are presented. Following, the force–displacement response and energy distribution of the simulation are shown.

Figures 11 and 12 present the mechanical behavior of two proposed FG re-entrant designs under loading and unloading, numerically. Parts (a)–(c) display configurations of the metastructures under loading–unloading obtained from numerical FEM, while part (d) depicts the force–displacement graph during loading and unloading. Part (d) also shows energies dissipated and absorbed in the loading–unloading step. For both FG re-entrants I and II, the force increases linearly with increasing displacement from 0 to 2 mm; see figures 11(d) and 12(d). Next, the transient behavior of hardening to softening is observed. However, the FG re-entrant II can withstand almost twice as much force as the FG re-entrant I at a displacement of 5 mm. After experiencing a 5 mm stroke, the loss of stability is observed in the FG re-entrant I, leading to a softening snap-through type of buckling. An observed fluctuation is observed in both structures right after going through the buckling phase; see figures 11(b) and 12(b). For FG re-entrant I, the plateau regime is not obvious, and the force has an increasing trend by increasing displacement, while there are fluctuations on the force–displacement curve. The plateau regime is obvious for FG re-entrant II, which can be due to the buckling of more re-entrant walls. Indeed, as can be seen in figure 12(b), buckling occurs in more numbers of re-entrant walls at the bottom of structures due to their higher length. By increasing the displacement, buckling occurs in more re-entrant unit cells at an almost constant force. Another possible reason is that in the FG re-entrant I, by moving down the upper indenter, the upper unit cells (close to the indenter) deform; therefore, the force does not transform to other unit cells. Regarding FG re-entrant II structures, the smaller unit cells close to the indenter require more force to deform. Therefore, the force transforms to other unit cells, and buckling occurs in larger re-entrant unit cells. The stress distribution in figures 11(b) and 12(b) is a compelling reason.

Numerical studies reveal that distinct geometries of mechanical metamaterial structures result in structural stiffening in the region of impact, which may be advantageous for applications that necessitate high-impact resistance. The peak forces obtained for FG re-entrant I and II are about 1250 and 1310 N, respectively. Mechanical hysteresis, defined by noncoincident loading–unloading curves, is found through mechanical unloading. The metamaterial boat fender recovers a portion of its initial shape, while residual strains in the auxetics indicate the energy dissipation caused by plastic deformations. Consequently, the input energy caused by the external force is converted into kinetic energy, and a portion of it is dissipated
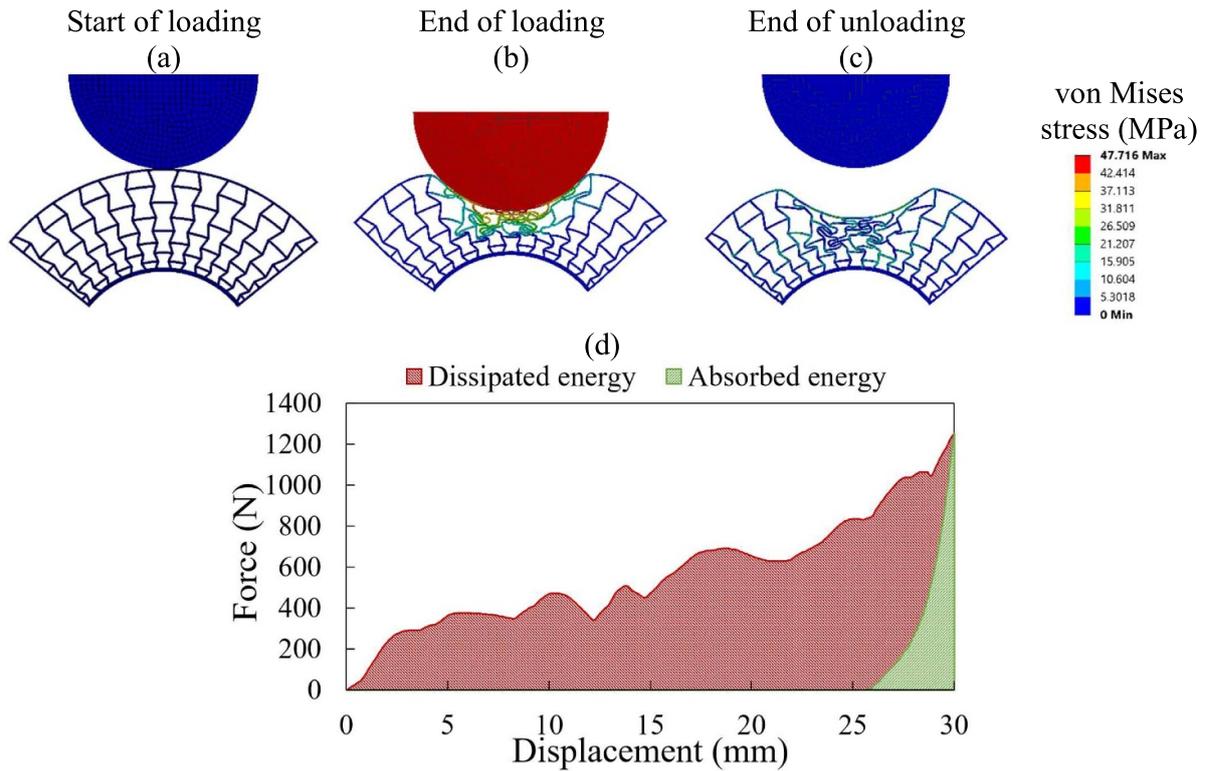
Figure 11. FG re-entrant I: (a)–(c) computational configuration of the lattice structure before loading, at the end of loading and unloading, and (d) force–displacement response during loading–unloading from FEM (dissipated and absorbed energies are denoted in red and green areas).
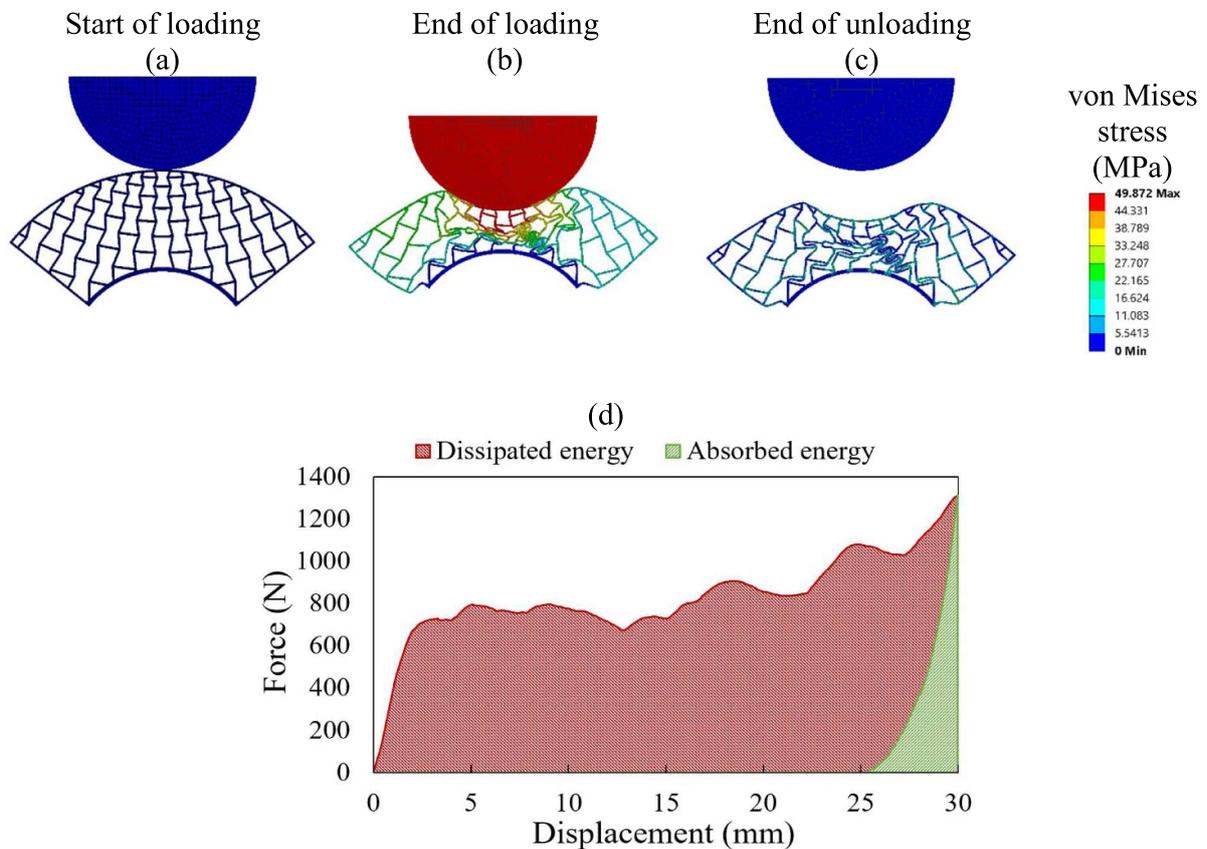
Figure 12. The counterpart of figure 11 for FG re-entrant II.
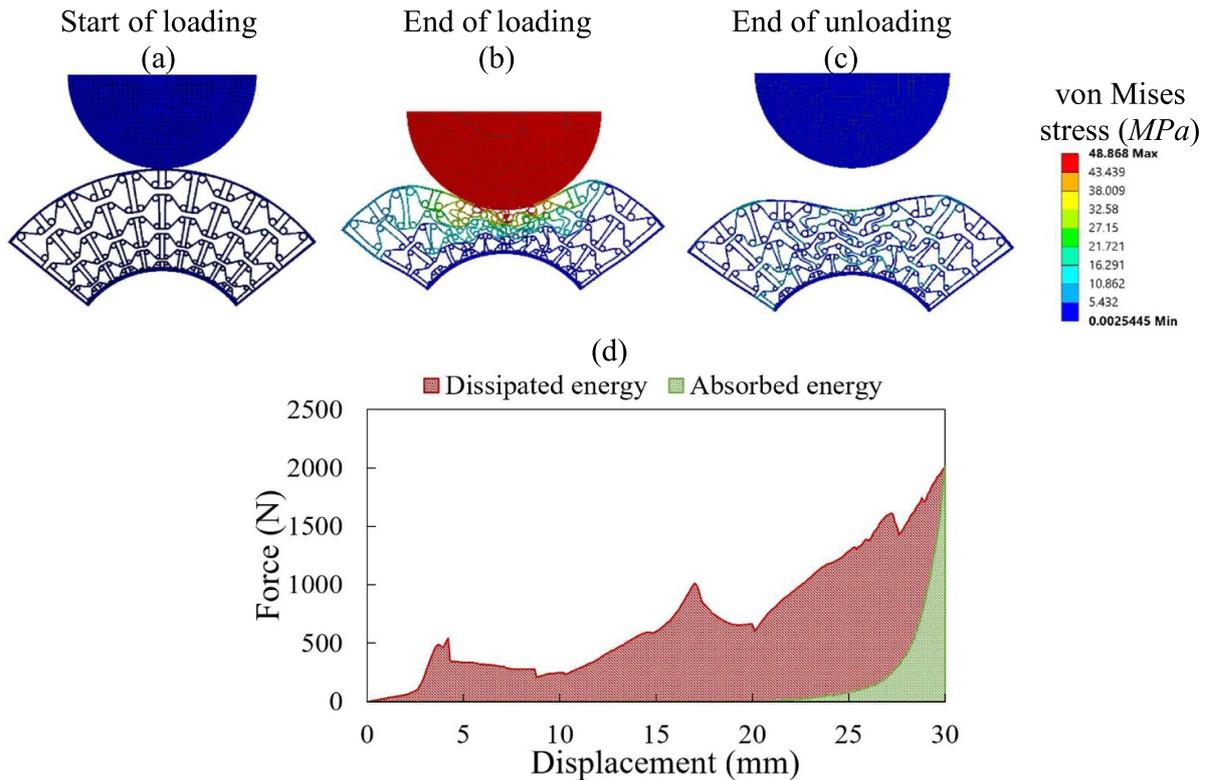
Figure 13. The counterpart of figure 11 for FG RCA I.

via the plastic deformation mechanism. When the distorted auxetic material was heated, it would regain its original form by releasing all plastic strains through a solid-state plastic-elastic phase transition. As discussed, the red area dissipates energy, and the green area absorbs energy through the lattice structure. The FG re-entrant lattices I and II have a shape fixity rate of 86.30% and 85.33%, respectively.

FG RCA I and II are the other two FG auxetic structure types examined now. Figures 13 and 14 present the mechanical behavior of two proposed FG RCA cylindrical panels under loading–unloading in a compressive mode. The FEM provides valuable results about the deformation, energy absorption/dissipation, and stability of these structures, which are crucial for designing proper boat fenders.

Figures 13 and 14(a)–(c) show numerical results of different FG RCAs I and II configurations from the rest condition to the end of loading and unloading, respectively. In FG RCA I, the re-entrant chiral cells are graded radially from small to larger unit cells. However, on the other hand, in FG RCA II, the unit cells are graded from large to small radially. Comparing figures 13(b), (c) and 14(b), (c) reveals that the FG RCA I is more stable under the compression load. Regarding the force response, the maximum force in the FG RCA II is almost 50% higher than the one for FG RCA I at the stroke of 30 mm; see part (d) of both figures. The force–displacement curve of FG RCA I, as presented in figure 13(d), reveals that the force–displacement curve has a linear trend at the small deformation, following the hardening behavior observed. At the stroke of 4 mm, a local snap-through type of buckling is prominent, in which the force drops with increasing the displacement.

After the first force drop, the force–displacement shows irregular softening–hardening cycles due to local bucking and densification phenomena happening in different areas and layers, mostly in the middle of the panel, as distal ends stay strong and less deformed. It is very clear that the center of the specimen experiences a localized layer collapse gradually. The densification regime begins when some of the members come into contact. The force–displacement curve of FG RCA II (figure 14(d)) shows that, after a linear regime followed by hardening, local buckling happens, and the force fluctuates with increasing the displacement leading to a plateau. After the plateau regime, dandification happens due to contact with re-entrant chiral walls. The dramatic fluctuation in the force plateau could be due to beam-like members' instability under compression load. A monotonically increasing trend is observed for the force after 17 mm displacement until the end of loading step. Finally, the FG RCA lattices I and II appear to result in a shape fixity rate of 68.03% and 77.56%, respectively.

In order to confirm that the fracture does not occur by moving down, ductile damage is defined in ABAQUS. In order to show the location and displacement of the damage initiation (and fracture) of boat fenders under applied load, the ductile damage initiation criterion (DUCTCRT) is reported by ABAQUS. DUCTCTR ranges from 0 to 1; when it reaches 1, the damage is initiated, and the structure loses its load-carrying ability [54]. Both experimental observation (naked eyes) and FEM show that the fracture does not occur by penetrating the upper indenter (for the maximum stroke of 30 mm) into the lattice structure for all boat-fender designs.
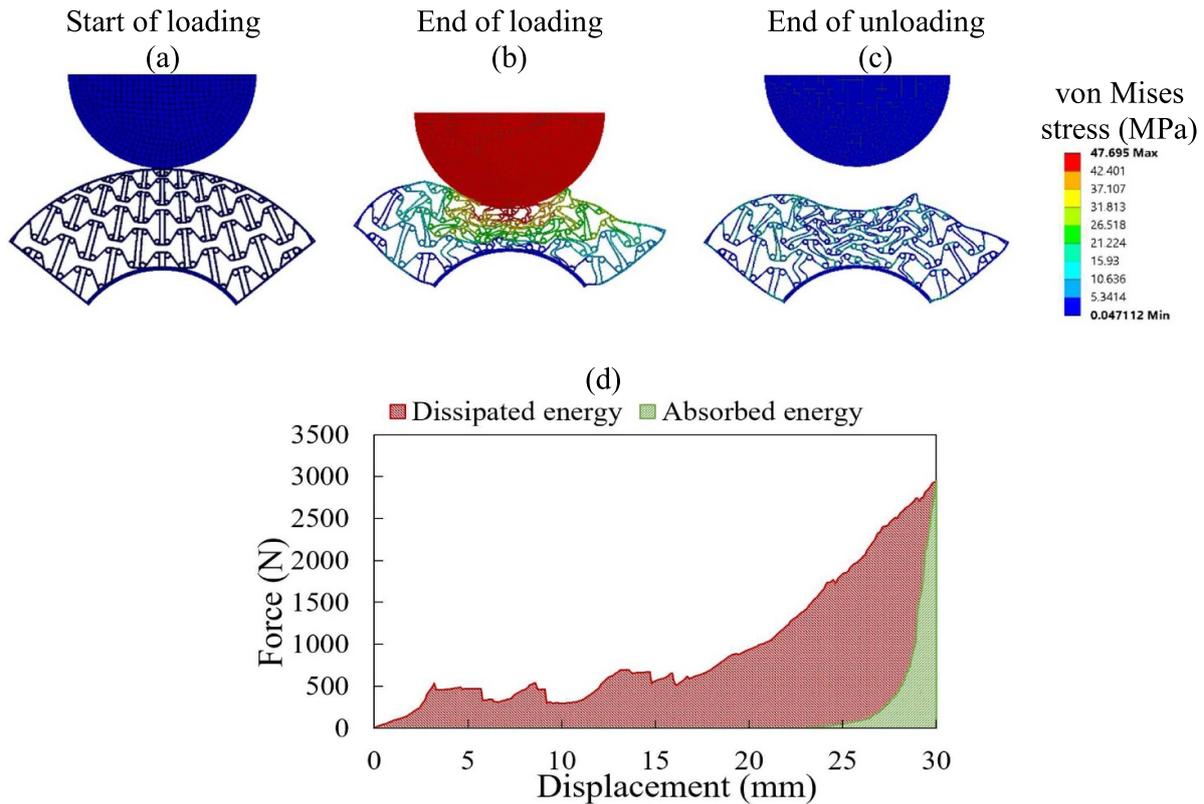
Figure 14. The counterpart of figure 11 for FG RCA II.

5. Discussion

5.1. Dissipation and absorption energies

It has also been found that 3D printing could help to freely create lattice structures with various unit cells and configurations depending on the force and displacement requirements. The results presented in the previous section could provide a guideline for creating lattices to meet design requirements. As observed, the density and pattern of unit cells, like gradients, play an important role in controlling the mechanical properties of the lattice structures.

As discussed already, the region contained by the loading and unloading curves represents the energy loss or dissipation mostly attributed to the plastic deformations and mechanical instability. The area under the unloading curve is considered absorbed energy due to the elastic deformations.

The force–displacement of lattice structures undergoing large deformation has three distinct stages. In the linear elastic stage, beam-like members simply bend elastically. The second stage, or plateau stage, is governed by three probable failure mechanisms of beam-like members: elastic buckling, plastic collapse, or brittle fracture. The final stage is densification, in which the force increases dramatically by increasing the applied displacement. The plateau stage is highly crucial for energy dissipation. Another important point is that the elastic energy stored by lattice structures is released after unloading, and if the lattice structures are not well-restricted, it may be harmful [55]. Therefore, the risks regarding the unloading stage should be assessed, and mitigation plans should be considered as well.

This section first reports both dissipated and absorbed energies for all designed structures in figure 15. This figure shows that the FG RCA II results in maximum energy dissipation and absorption. Moreover, the uniform honeycomb has the minimum energy dissipation and absorption. As illustrated in this figure, the amount of energy dissipation and absorption obtained from the experimental and numerical studies has an insignificant difference. The maximum difference between experiments and FEM for energy dissipation is almost 5%, and for energy absorption is nearly 17%.

In all investigated lattice structures in the present study, the energy dissipation is higher than the energy absorption. For example, in a uniform honeycomb, the energy dissipation is 18 times higher than the energy absorption. More energy is dissipated than absorbed for this lattice structure due to the plastic hardening properties of both PLA and lattice structure. Figure 15 also reveals that a FG honeycomb dissipates more energy. The FG honeycomb type II dissipates 44% and absorbs 73% more energy compared to the uniform honeycomb. Moreover, lattice structure type II, in which the unit cells become smaller radially, dissipates more energy compared to type I, in which the unit cells become larger in the radial direction. For example, the FG honeycomb type II dissipates 17% more energy than the FG honeycomb type I. Therefore, making lattice structure graded increases both energy dissipation and absorption.

(a)

(b)
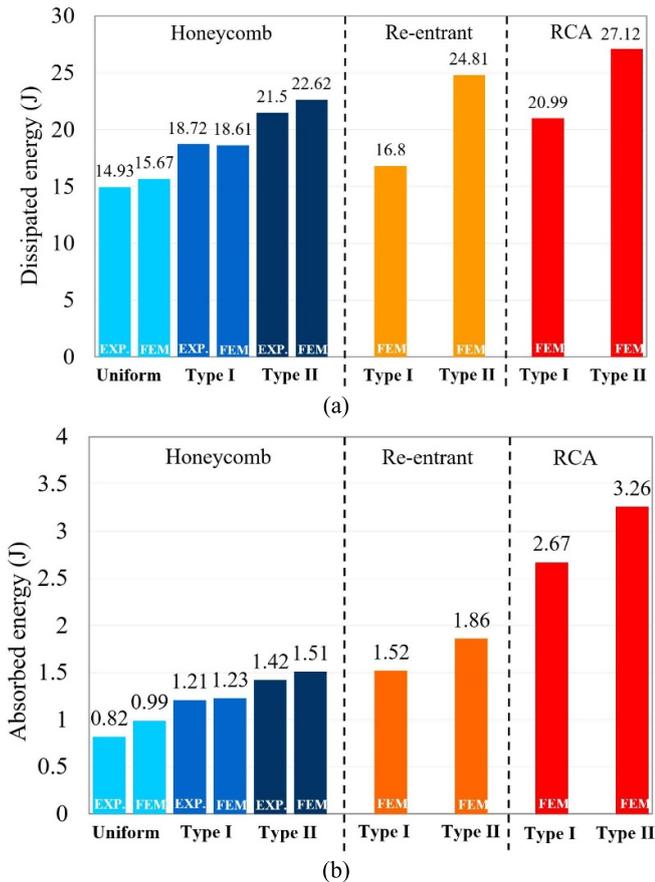
Figure 15. (a) Energy dissipation and (b) energy absorption capacity of the investigated metamaterials.

(a)

(b)

Figure 16. (a) Configuration of FG honeycomb II after heating–cooling at the end of the second loading–unloading cycle, (b) experimental force–displacement response during two cycles of loading–unloading-heating–cooling.

It is worth mentioning that the FG design is advantageous only for a specific loading condition, such as a normal loading condition, the same as the present study. Niknam and Akbarzadeh [56], show that the gradient design, where the relative density normally varies in the direction of external compressive force, increases a cellular structure's energy absorption capabilities by 110%. Therefore, the direction of loading in the FG structures is highly crucial, and in other loading conditions, the desirable mechanical properties might decrease.

Moreover, in this loading condition, the direction of the graded core is crucial as the re-entrant type II dissipates more energy than type I. The honeycomb type II and RCA type II have the same trend as the re-entrant.

5.2. Mechanical properties recovery

The shape and mechanical properties recovery are two main aspects of shape memory recovery of metastructures in crashworthiness applications. In section 4, the shape recovery of metastructures has been investigated for one cycle of loading–unloading-heating–cooling. This section examines the mechanical properties recovery of metastructures, which entails applying a cycling loading (two cycles of loading–unloading-heating–cooling). The FG honeycomb II boat fender experiences a loading–unloading with plastic deformations followed

by heating and cooling in cycle 1 showing a full shape recovery. The structure is then compressed in cycle 2 followed by an unloading stage leading to a residual plastic deformation at the end. Figure 16(a) presents the configuration of the FG honeycomb II after the second heating–cooling revealing a full shape recovery. Figure 16(b) shows the force–displacement response of the FG honeycomb II boat fender under loading–unloading for cycles 1 and 2 with a maximum displacement of 30 mm. As can be seen, the force–displacement curve of cycle 2 has almost the same path/trend as cycle 1. The linear stage for each cycle has almost the same slope. cycle 2 results in a similar plateau regime as cycle 1, while the maximum load that the structure undergoes in cycle 2 is slightly lower than that of cycle 1 at the same applied stroke. Figure 16(b) proves an excellent level for the mechanical properties recovery of FG honeycomb II boat fender. It implies that the structure is safe and viable to be used again. It is worth mentioning that the same cyclic loading is applied to FG re-entrant I and an excellent mechanical properties recovery is found, but it is not reported here for the sake of brevity.

5.3. Feasibility of proposed design

This section examines the feasibility of the proposed novel boat fender according to Fender Application Design Manual [46, 53]. According to [46], the normal berthing energy is deciding factor in designing and selecting the most efficient fender. Normal berthing energy is defined as:

Table 1. Specific energy dissipation for different lattice boat fenders.

	Uniform honeycomb	FG honeycomb I	FG honeycomb II	FG re-entrant I	FG re-entrant II	FG RCA I	FG RCA II
Mass (g)	18.90	19.47	20.04	20.89	20.99	24.28	23.47
SED (J g^{-1})	0.83	0.96	1.13	0.80	1.18	0.86	1.15

$$E_{\mathrm{N}} = 0.5 \times M_{\mathrm{D}} \times V_{\mathrm{B}}{}^2 \times C_{\mathrm{M}} \times C_{\mathrm{E}} \times C_{\mathrm{C}} \times C_{\mathrm{S}} \qquad (1)$$

where,

$E_{\mathrm{N}} =$ Normal berthing energy to be absorbed by the fender (J)

$M_{\mathrm{D}} =$ Mass of the boat

$V_{\mathrm{B}} =$ Approach velocity component perpendicular to the berthing line (m s^{-1})

$C_{\mathrm{M}} =$ Added mass coefficient

$C_{\mathrm{E}} =$ Eccentricity coefficient

$C_{\mathrm{C}} =$ Berth configuration coefficient

$C_{\mathrm{S}} =$ Softness coefficient

All parameters in equation (1) are calculated considering that the boat in the current project is a deck boat. Therefore, according to [46]:

$$M_{\mathrm{D}} = \mathrm{LWT} + \mathrm{DWT} = 1400 + 500 = 1900 \ \mathrm{kg}$$

where LWT is the weight of the boat, and DWT is the weight of cargo, crew or fuel.

There are several berthing types, but the most common is slide berthing. According to [46], in the case of good berthing and for normal boats, $V_{\mathrm{B}} = 0.1$ m s^{-1}. Although for the worst case, difficult berthing (sheltered) $V_{\mathrm{B}} = 0.35$ m s^{-1}. The present study considers the worst case of designing a boat fender.

C_{M} depends on the boat's geometry, which must always be less than 1. For a deckboat it is close to $C_{\mathrm{M}} = 0.6$.

The eccentricity coefficient (C_{E}) accounts for the energy dissipated by the ship's rotation about its point of impact with the fenders, in the worst case of berthing $C_{\mathrm{E}} = 1$.

The berth configuration coefficient considers the amount of energy dissipated by water during berthing as the closed form is considered here, $C_{\mathrm{C}} = 0.9$.

For the soft fender, exactly the same as the current fender, $C_{\mathrm{S}} = 1$.

Therefore $E_{\mathrm{N}} = 125.68$ J.

This amount of energy induced by the boat must be carried out using a well-designed boat fender. As discussed in figure 15, re-entrant type II can dissipate almost 24 J. It is worth mentioning that this structure has a thickness of 10 mm, therefore, several re-entrant boat fenders can be employed to absorb the kinetic energy induced by boats.

5.4. Comparison of present designs with available cellular designs

Recently, mass reduction in the engineering structure has been highlighted due to issues related to fossil fuel consumption and environmental problems. Therefore, in the sustainable design of lattice structures for recoverable boat fenders, both energy absorption/dissipation and the overall mass must be considered. Here, the energy dissipation per unit mass, so-called specific energy dissipation (SED in J g^{-1}), is discussed. According to Yousefi *et al* [3], it is defined by the following equation (2):

$$\mathrm{SED} = \frac{\mathrm{Energy \ dissipation}}{\mathrm{Structure \ mass}}. \qquad (2)$$

Energy dissipation per unit mass (i.e., SED) is a key factor in designing lattice structures, which is reported in table 1. As can be seen from table 1, the FG RCA has the maximum mass, and the uniform honeycomb has the minimum mass. According to table 1, the FG honeycomb type II, FG re-entrant type II, and FG RCA type II are potential candidates for designing boat-fendering systems, considering their high energy dissipation per unit mass. It is worth mentioning that the FG re-entrant type II has the maximum SED, making it unique among the other designs. Therefore, it is found that FG boat fenders possess desirable results regarding SED.

Different playing factors, like deformation/force level, shape recovery rate, shape fixity rate, energy dissipation, energy absorption, SED, boat type and operational conditions, should be considered for designing a safe and efficient boat fender. As there are many factors, sometimes considering the most important factor is the easiest way but not the best. For example, if energy dissipation and mass are crucial factors, the FG re-entrant II is a desired lattice. Applying the multi-objective optimization method would be very beneficial for finding an optimal design that could be considered for future research developments.

The SED is a crucial parameter for designing energy absorption/dissipation structures. In this regard, the maximum and minimum amount of SED calculated in the present structure is 1.18 J g^{-1} and 0.80 J g^{-1}, respectively. Serjouei *et al* [4] reported specific energy absorption per unit mass for hexagonal horseshoe shape and square horseshoe shape cellular designs, as 0.069 J g^{-1} and 0.062 J g^{-1}. In addition, Yousefi *et al* [3] reported this parameter for both soft and hard bio-inspired 3D star-triangular auxetic honeycomb (3DSTH), as 0.0543 J g^{-1} and 0.616 J g^{-1}, respectively. By comparing present designs with these available designs, it can be concluded that present designs are highly efficient regarding SED.

6. Summary and concluding remarks

The boat fender is a crucial structural part of boats. It helps to slowly stop the boat and avoid damage during mooring. In the present study, a new class of fendering systems with excellent

energy absorption/dissipation and shape recovery was introduced and fabricated by 4D printing technology. Novel engineering types of lattice structures with high energy absorption/dissipation capability were employed to design advanced fendering systems. The functionally gradient concept was also applied to designs to reach efficient structures. This research work investigated the mechanical deformation, shape recovery, shape fixity rate, energy dissipation/absorption, and energy dissipation per unit mass for seven metamaterial lattice structures via experimental and numerical studies. The following main results can be concluded:

- The developed FEM can replicate the experimental observations with acceptable accuracy.
- The FG structure increases the maximum loads that the boat-fendering lattice could withstand. For example, the maximum load withstood by FG honeycomb is increased by 66% compared to the uniform form.
- The FG pattern with specific unit cells can change the deformation pattern and, subsequently, the force–displacement response to a desired one.
- The lattice pattern in the boat fender structures is found to be crucial. The FG lattice, for instance, increases the energy dissipation. It is seen that making re-entrant fender graded enhances energy dissipation levels by 47%.
- FG honeycomb II possesses a maximum shape fixity of 90.36%, and FG RCA I results in a minimum shape fixity of 68.03%.
- PLA materials and structures introduced in this research can recover their original shape. All boat fenders 4D printed in this work show 100% shape recovery. Therefore, the 4D-printed boat fenders could remove the need for part replacement, promote sustainability and lower the waste of materials, time, energy, and labor need.
- FG re-entrant II has the maximum SED, and the uniform honeycomb has the minimum SED.
- The current model is a small-scale model of metamaterial boat fenders. Fabrication of boat fenders would need a large-scale 3D printer enabling full-scale prototyping.
- Cyclic loading applied to the boat fender proves an excellent recovery of mechanical properties. Results show the capability of novel boat fenders to be used several times.

Data availability statement

All data that support the findings of this study are included within the article (and any supplementary files).

ORCID iDs

Mahdi Bodaghi ● https://orcid.org/0000-0002-0707-944X
Naser Namvar ● https://orcid.org/0009-0009-7127-0706
Armin Yousefi ● https://orcid.org/0000-0001-7478-7991
Frédéric Demoly ● https://orcid.org/0000-0002-5825-6573
Ali Zolfagharian ● https://orcid.org/0000-0001-5302-360X

References

[1] Eshkoor R A, Oshkovr S A, Sulong A B, Zulkifli R, Ariffin A K and Azhari C H 2013 Comparative research on the crashworthiness characteristics of woven natural silk/epoxy composite tubes *Mater. Des.* **47** 248–57

[2] Mohammadi I, Haghighi-Yazdi M, Safarabadi M and Yousefi A 2023 Crashworthiness analysis of a composite guardrail under impact loading *Proc. Inst. Electr. Eng.* L **237** 1651–64

[3] Yousefi A, Jolaiy S, Lalegani Dezaki M, Zolfagharian A, Serjouei A and Bodaghi M 2023 3D-printed soft and hard meta-structures with supreme energy absorption and dissipation capacities in cyclic loading conditions *Adv. Eng. Mater.* **25** 2201189

[4] Serjouei A, Yousefi A, Jenaki A, Bodaghi M and Mehrpouya M 2022 4D printed shape memory sandwich structures: experimental analysis and numerical modeling *Smart Mater. Struct.* **31** 055014

[5] Sadegh Ebrahimi M, Hashemi R and Etemadi E 2022 In-plane energy absorption characteristics and mechanical properties of 3D printed novel hybrid cellular structures *J. Mater. Res. Technol.* **20** 3616–32

[6] Jazar R N and Dai L 2016 *Nonlinear Approaches in Engineering Applications: Advanced Analysis of Vehicle Related Technologies* (Springer)

[7] Hedayati R, Yousefi A and Bodaghi M 2022 Sandwich structures with repairable cores based on truncated cube cells *Composites* B **243** 110124

[8] Hamzehei R, Rezaei S, Kadkhodapour J, Anaraki A P and Mahmoudi A 2020 2D triangular anti-trichiral structures and auxetic stents with symmetric shrinkage behavior and high energy absorption *Mech. Mater.* **142** 103291

[9] Saxena K K, Das R and Calius E P 2016 Three decades of auxetics research− materials with negative Poisson's ratio: a review *Adv. Eng. Mater.* **18** 1847–70

[10] Kadic M, Milton G W, van Hecke M and Wegener M 2019 3D metamaterials *Nat. Rev. Phys.* **1** 198

[11] Hedayati R, Yousefi A, Dezaki M L and Bodaghi M 2023 Analytical relationships for 2D re-entrant auxetic metamaterials: an application to 3D printing flexible implants *J. Mech. Behav. Biomed. Mater.* **143** 105938

[12] Zhai Z, Wang Y and Jiang H 2018 Origami-inspired, on-demand deployable and collapsible mechanical metamaterials with tunable stiffness *Proc. Natl Acad. Sci.* **115** 2032–7

[13] Wang Q *et al* 2016 Lightweight mechanical metamaterials with tunable negative thermal expansion *Phys. Rev. Lett.* **117** 175901

[14] Dudek K, Gatt R, Dudek M R and Grima J N 2018 Negative and positive stiffness in auxetic magneto-mechanical metamaterials *Proc. R. Soc.* A **474** 20180003

[15] Krushynska A, Galich P, Bosia F, Pugno N M and Rudykh S 2018 Hybrid metamaterials combining pentamode lattices and phononic plates *Appl. Phys. Lett.* **113** 201901

[16] Babaee S, Shim J, Weaver J C, Chen E R, Patel N and Bertoldi K 2013 3D soft metamaterials with negative Poisson's ratio *Adv. Mater.* **25** 5044–9

[17] Zadpoor A A 2016 Mechanical meta-materials *Mater. Horiz.* **3** 371–81

[18] Ngo T D *et al* 2018 Additive manufacturing (3D printing): a review of materials, methods, applications and challenges *Composites* B **143** 172–96

[19] Tibbits S 2014 4D printing: multi-material shape change *Archit. Des.* **84** 116–21

[20] Ge Q, Qi H J and Dunn M L 2013 Active materials by four-dimension printing *Appl. Phys. Lett.* **103** 131901

[21] Demoly F and Andre J-C 2022 *4D Printing, Volume 1: Between Disruptive Research and Industrial Applications* (Wiley)

[22] Demoly F *et al* 2021 The status, barriers, challenges, and future in design for 4D printing *Mater. Des.* **212** 110193

[23] Demoly F and Andre J-C 2022 *4D Printing, Volume 2: Between Science and Technology* (Wiley)

[24] Tao R, Xi L, Wu W, Li Y, Liao B, Liu L, Leng J and Fang D 2020 4D printed multi-stable metamaterials with mechanically tunable performance *Compos. Struct.* **252** 112663

[25] Tao R, Ji L, Li Y, Wan Z, Hu W, Wu W, Liao B, Ma L and Fang D 2020 4D printed origami metamaterials with tunable compression twist behavior and stress-strain curves *Composites* B **201** 108344

[26] Lendlein A and Langer R 2002 Biodegradable, elastic shape-memory polymers for potential biomedical applications *Science* **296** 1673–6

[27] Pilate F, Toncheva A, Dubois P and Raquez J-M 2016 Shape-memory polymers for multiple applications in the materials world *Eur. Polym. J.* **80** 268–94

[28] Small W IV, Singhal P, Wilson T S and Maitland D J 2010 Biomedical applications of thermally activated shape memory polymers *J. Mater. Chem.* **20** 3356–66

[29] Mahdi Rafiee M, Baniassadi M, Wang K, Baniasadi M and Baghani M 2021 Mechanical properties improvement of shape memory polymers by designing the microstructure of multi-phase heterogeneous materials *Comput. Mater. Sci.* **196** 110523

[30] Namvar N, Zolfagharian A, Vakili-Tahami F and Bodaghi M 2022 Reversible energy absorption of elasto-plastic auxetic, hexagonal, and AuxHex structures fabricated by FDM 4D printing *Smart Mater. Struct.* **31** 055021

[31] Hamzehei R, Serjouei A, Wu N, Zolfagharian A and Bodaghi M 2022 4D metamaterials with zero Poisson's ratio, shape recovery, and energy absorption features *Adv. Eng. Mater.* **24** 2200656

[32] Sharma D and Hiremath S S 2023 Experimental and FEM study on the in-plane and out-plane loaded reversible dual-material bio-inspired lattice structures with improved energy absorption performance *Compos. Struct.* 116353

[33] Wu Y, Sun L, Yang P, Fang J and Li W 2021 Energy absorption of additively manufactured functionally bi-graded thickness honeycombs subjected to axial loads *Thin-Walled Struct.* **164** 107810

[34] Xu F, Zhang X and Zhang H 2018 A review on functionally graded structures and materials for energy absorption *Eng. Struct.* **171** 309–25

[35] Alshaqaq M and Erturk A 2020 Graded multifunctional piezoelectric metastructures for wideband vibration attenuation and energy harvesting *Smart Mater. Struct.* **30** 015029

[36] Novak N, Borovinšek M, Vesenjak M, Wormser M, Körner C, Tanaka S, Hokamoto K and Ren Z 2019 Crushing behavior of graded auxetic structures built from inverted tetrapods under impact *Phys. Status Solidi* b **256** 1800040

[37] Li Z, Jiang Y, Wang T, Wang L, Zhuang W and Liu D 2019 In-plane crushing behaviors of piecewise linear graded honeycombs *Compos. Struct.* **207** 425–37

[38] Hamzehei R, Zolfagharian A, Dariushi S and Bodaghi M 2022 3D-printed bio-inspired zero Poisson's ratio graded metamaterials with high energy absorption performance *Smart Mater. Struct.* **31** 035001

[39] Spencer T E 2004 Marine fender systems, in ports 2004: port development in the changing world pp 1–10

[40] Fan W, Yuan W and Chen B 2015 Steel fender limitations and improvements for bridge protection in ship collisions *J. Bridge Eng.* **20** 06015004

[41] Sakakibara S and Kubo M 2007 Ship berthing and mooring monitoring system by pneumatic-type fenders *Ocean Eng.* **34** 1174–81

[42] Lee T T 1968 Design critria recommended for marine fender systems *Coast. Eng. Proc.* **1** 1159–84

[43] Voyiadjis G Z, El-Tawil S and Kocke P J 2008 *Feasibility of Tubular Fender Units for Pier Protection against Vessel Collision* Louisiana State University. Department of Civil and Environmental Engieering (available at: https://rosap.ntl.bts.gov/view/dot/22096/dot_22096_DS1.pdf)

[44] Bodaghi M, Serjouei A, Zolfagharian A, Fotouhi M, Rahman H and Durand D 2020 Reversible energy absorbing meta-sandwiches by FDM 4D printing *Int. J. Mech. Sci.* **173** 105451

[45] Guo X, Liu L, Zhou B, Liu Y and Leng J 2015 Influence of strain rates on the mechanical behaviors of shape memory polymer *Smart Mater. Struct.* **24** 095009

[46] Infrastructure T M A 2022 *Fender Application Design Manual* (Trelleborg) (available at: www.trelleborg.com/marine-and-infrastructure/-/media/marine-systems/resources/guides-and-design-manual/downloads/fender-application-design-manual.pdf?rev=f3e34525d9ee4331b058f46f0ec489f4)

[47] Alomarah A, Masood S H, Sbarski I, Faisal B, Gao Z and Ruan D 2020 Compressive properties of 3D printed auxetic structures: experimental and numerical studies *Virtual Phys. Prototyp.* **15** 1–21

[48] Yuan S, Chua C K and Zhou K 2019 3D-printed mechanical metamaterials with high energy absorption *Adv. Mater. Technol.* **4** 1800419

[49] Li D, Liao W, Dai N and Xie Y M 2019 Comparison of mechanical properties and energy absorption of sheet-based and strut-based gyroid cellular structures with graded densities *Materials* **12** 2183

[50] Yang L, Harrysson O, West H and Cormier D 2015 Mechanical properties of 3D re-entrant honeycomb auxetic structures realized via additive manufacturing *Int. J. Solids Struct.* **69** 475–90

[51] Wang X-T, Li X-W and Ma L 2016 Interlocking assembled 3D auxetic cellular structures *Mater. Des.* **99** 467–76

[52] Baran T and Öztürk M 2020 In-plane elasticity of a strengthened re-entrant honeycomb cell *Eur. J. Mech.* A **83** 104037

[53] Lu Z-X, Li X, Yang Z-Y and Xie F 2016 Novel structure with negative Poisson's ratio and enhanced Young's modulus *Compos. Struct.* **138** 243–52

[54] ABAQUS H 2014 *ABAQUS Standard User's Manual, Version 6.14* (Dassault Systèmes)

[55] Lu G and Yu T 2003 *Energy Absorption of Structures and Materials* (Elsevier) (https://doi.org/10.1038/nmat877)

[56] Niknam H and Akbarzadeh A 2020 Graded lattice structures: simultaneous enhancement in stiffness and energy absorption *Mater. Des.* **196** 109129